ACS OMEGA

Open Access

http://pubs.acs.org/journal/acsodf

Article

Numerical Assessment of Combustion Behavior and Emission Formations in an Ultrasonic-Assisted Ignition Engine

Shiwei Zhang, Cheng Shi, and Liming Di*

Cite This: *ACS Omega* 2023, 8, 36418−36434

Read Online

ACCESS | Metrics & More | Article Recommendations

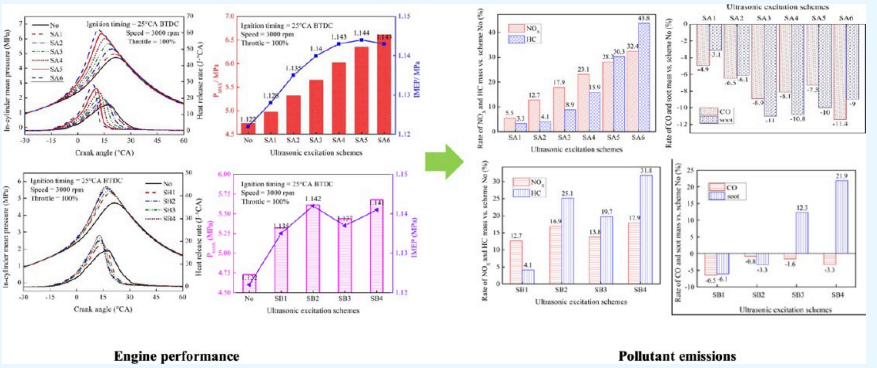

ABSTRACT: By effective utilization of the dynamic mesh and coordinate transformation techniques, an ultrasonic horn is physically integrated in the chamber of an internal combustion engine. The consequences of multiple ultrasonic-fed strategies on the flow field, combustion process, and emission formation under the same working conditions are studied by numerical simulation. Based precisely on the bench test data, GT-Power and CONVERGE set up the original engine one-dimension (1d) and three-dimension (3d) simulation models. The chamber pressure and heat release rate of the 1d and 3d models under a full load condition of 3000 r·min^{-1} were validated, and the maximum relative error is less than 5%, proving the accuracy of the model. By reforming the 3d numerical model, ultrasonics is added to the gasoline engine's combustion chamber. Six different ultrasonic-fed schemes with 20 kHz amplitude of 30−300 μm are typically selected for in-depth research. The larger the amplitude, the stronger the turbulent kinetic energy (TKE), and the maximum TKE exceeds 46.6% at the ignition time. Stronger TKE can energetically encourage the generation of OH, O, and H radicals and improve the combustion reaction rate, and the peak pressure (P_{MAX}) is increased by 1.9 MPa compared with scheme No. However, NO_X and HC emissions gradually increase, reaching a maximum of 32.4 and 43.8%, respectively, while CO and soot emissions decrease, reaching a maximum of 11.4 and 11%, respectively. Four groups of ultrasonic-fed schemes with an amplitude of 100 μm and frequency of 20−50 kHz are scientifically studied. The findings indicated that the TKE level steadily increases as the frequency increases and the in-cylinder TKE increases by 16.4% at ignition time. The increase in ultrasonic frequency can promote the generation of active free radicals and meaningfully improve the combustion reaction rate to a certain extent. The P_{MAX} can be increased up to 1 MPa compared with scheme No. At the same time, the NO_X, HC, and soot also increased considerably, reaching 31.8, 17.9, and 21.9%, respectively. The CO showed a downward trend but gradually slowed, with a maximum decline of 6.5% at 20 kHz. The above simulation analysis is based on the full load condition of 3000 r·min^{-1}, sufficiently proving that ultrasonics has a regulation effect on emissions and can achieve specific emissions through later optimization.

1. INTRODUCTION

In 2020, Chinese President Xi Jinping willingly promised the world to peak carbon emissions by 2030 and become carbon neutral by 2060 at the United Nations General Assembly. Burning fossil fuels is one of the leading causes of soaring CO_2 levels in the atmosphere, according to the Carbon Dioxide Information Analysis Centre.[1] Furthermore, according to extensive research by the World Meteorological Organization, the surge of greenhouse gases such as CO_2 in the atmosphere is a fundamental reason for abnormal global climate change.[2] In recent years, the rapid increase in civil car ownership has intentionally caused a series of energy and environmental crisis.[3,4] In response to the intractable energy and environmental crisis, legitimate governments worldwide have enacted stringent

Received: July 25, 2023
Accepted: September 1, 2023
Published: September 22, 2023

https://doi.org/10.1021/acsomega.3c05415
ACS Omega 2023, 8, 36418−36434

regulations on vehicle emissions.[5,6] Clean combustion is one of the current research hotspots. Also, acoustic excitation has a significant effect on improving combustion quality and reducing pollutant emissions. This study is based on the combustion process in gasoline engines under ultrasonic action to explore and expand the influence of acoustic excitation on the combustion process of flammable fuel in extremely high-speed transient environments.

The advanced combustion technology of the internal combustion engine is necessary to solve the crisis of human energy and the environment. An ultrasonic wave is a very short wavelength wave with a frequency above 20 kHz. The shorter wavelength gives it better anisotropy, which is used in ultrasonic flaw detection and ultrasonic imaging technology. Ultrasonic welding, drilling, and crushing can be carried out using the mechanical effect. When the ultrasonic wave propagates in the liquid medium, a large number of microbubbles will be produced. Because of the effect of ultrasonics, the microbubbles will have an alternating period of positive and negative pressure, which makes the bubbles grow until they burst. When bubbles burst, a shock wave will be naturally generated, which plays a good role in stirring, and the internal friction between dielectrics will form a charge and discharge in the bubble to produce luminescence, accompanied by high temperature and pressure. In addition, under the continuous action of ultrasonic, the internal temperature of the medium will rise significantly because of the sound energy absorption and internal friction of the medium.[7−9] Typically, the media might experience complicated chemical, physical, and other consequences as a result of the ultrasonic effects.[10,11] The widespread use of ultrasonic in many different fields has demonstrated that it has very powerful advantages.[12−14]

The application of acoustic excitation may significantly enhance the combustion performance of the flame. To determine how acoustic excitation affected flame behavior, Fujisawa et al.[15] carried out a visual flow research on the diffusion flame. The findings revealed that under an acoustic excitation of 100−300 Hz, the velocity and temperature increase, and under low amplitude acoustic excitation, flame height and flame amplitude decrease slightly, and flame scintillation behavior remains unchanged. The flame switches from laminar to swirl flow due to the creation of asymmetric vortex rings near the combustion chamber exit under high-amplitude acoustic excitation, resulting in a dramatic fall in the flame height, amplitude, and flame luminosity. Jocher et al.[16] investigated the effect of acoustic forcing on the formation of soot and temperature in an ethylene−air flame. The results showed that as the frequency increased, the soot peak value decreased. At 20 kHz, the influence of buoyancy acceleration of the combustion gas may play a part in soot formation. At 40 kHz, soot formation is primarily controlled by flow forces. Oh et al.[17] investigated the effect of acoustic excitation on NO_X reduction and flame stability in a lifted nonpremixed turbulent hydrogen jet with coaxial air. The findings disclosed that the NO_X emissions decrease most at the resonant frequency under an acoustic excitation of 150−1000 Hz. Vortices generated by acoustic forcing promote entrainment of air, increasing the fuel−air mixing rate, and this premixing effect leads to lower flame temperature, thus reducing NO_X emissions. The effects of acoustic excitation, reburn, and postflam air on CO and NO_X emissions in the burning of premixed propane were examined by Hassan et al.[18] The findings demonstrated that the most efficient strategy for reducing NO_X concentration is acoustic excitation combined with postjet reburning, which reduces the NO_X formation by the premixed flame by 95%. Deng et al. explored the influence of acoustic excitation on NO decrease during methane combustion. By comparing NO_X emission, it is found that pulsating combustion caused by acoustic excitation makes NO_X emission less. This is primarily because the pulsating combustion causes the peak combustion temperature to decrease and makes the temperature distribution more balanced.[19] Moreover, different acoustic parameters significantly impact on partially premixed flame NO_X emissions.[20] Pereira et al.[21] reduced the emissions of NO_X, CO, formaldehyde, and acetaldehyde by using acoustic excitation and oxygen-enhanced combustion technology and significantly improved the combustion efficiency. Ion et al.[22] researched the influence of ultrasonic on the combustion behavior of gas burners. The findings demonstrated that ultrasonics enhances combustion efficiency and lower NO_X and CO emissions and results in a more uniform combustion temperature. The above research indicates that acoustic excitation plays an important role in improving combustion efficiency and reducing pollutant formation, but the mechanism of its impact on combustion is still unclear and the frequency range is below the ultrasonic frequency. Long and Guo[23] used a high-speed camera, Schlieren apparatus, and laser-induced fluorescence method to analyze the droplet combustion process in the ultrasonic field. The results showed that ultrasonic significantly affects on flame shape, combustion rate, and free radical distribution. Also, on droplet combustion, ultrasonic nodes and antinodes have quite varied effects. Di et al.[24] explored the ignition characteristics based on spherical focusing ultrasonic. The findings revealed that the frequency of the sound source is 300 kHz. The temperature rise of ultrasonic spherical focus is 299.87 K and the sound intensity is 3.4×10^9 W/m^2. The sound pressure is 3.02 MPa, which can meet the critical ignition point of gasoline, diesel, and other conventional fossil fuels. Di et al.[25] studied the influence of ultrasonic-fed time on combustion behavior and emission formations in a gasoline engine. The results demonstrated that the effect on combustion performance increased with increasing ultrasonic-fed time. With increasing ultrasonic-fed time, the consequence of ultrasonics on combustion is significant, decreasing CO and soot while rising NO_X. Research on the effect of ultrasonic on combustion is relatively rare, and the literature[23−25] indicates that ultrasonic significantly impacts the improvement of combustion rate and the formation of pollutants. Therefore, extending the acoustic excitation frequency to the ultrasonic frequency is of great significance, which can fill the gap in this field and provide relevant data references for subsequent research.

At present, it has not been discovered that ultrasonic is supplied straight into the engine's combustion chamber to investigate its effect on the in-cylinder flow field distributions, combustion process, and emission formations. In this study, the internal combustion engine was ultrasonic-fed as the research object, a multiphysical field simulation model of acoustic field and combustion field coupling was set up, and the CONVERGE software dynamic grid function was properly used to realize the ultrasonic feed into the gasoline engine's combustion chamber. This paper reveals precisely the influence mechanism of constant frequency variable amplitude ultrasonic and variable frequency constant amplitude ultrasonic on mixed flow, combustion evolution, and emission formation of gasoline engines, solves the related scientific problems faced by

https://doi.org/10.1021/acsomega.3c05415
ACS Omega 2023, 8, 36418−36434

traditional internal combustion engines, and provides theoretical guidance for efficient and clean combustion.

2. CFD MODEL ESTABLISHMENT

2.1. Model Construction and Grid Realization. CONVERGE software has excellent dynamic grid processing ability, so this software is naturally chosen to build a 3d simulation model. Furthermore, CATIA software is selected for reverse modeling the Honda WH125-6 engine. The 3d simulation model needs the 1d simulation model to provide data reference. Therefore, GT-Power software creates the 1d simulation model based on the original engine's structural characteristics and bench test results. The 1d transient inlet pressure, transient inlet temperature, and other boundary parameters are used as the reference condition for 3d simulation. The basic parameters of the Honda WH125-6 engine are listed in Table 1.

Table 1. Basic Parameters of Honda WH125-6 Engine

basic parameters	description
engine type	single-cylinder
piston stroke (mm)	57.9
cylinder displacement (mL)	124.8
compression ratio	9.0
maximum torque (N·m)	9.68 (3500 r·min^{-1})
maximum power (kW)	6.6 (7000 r·min^{-1})

In computational fluid dynamics (CFD) simulations, grid division plays a crucial role, so the in-cylinder mean pressure is tested for grid independence at various grid scales. Under the condition that other encryption criteria remain unchanged, only the basic grid size is changed and set to 3, 4, and 5 mm. Figure 1

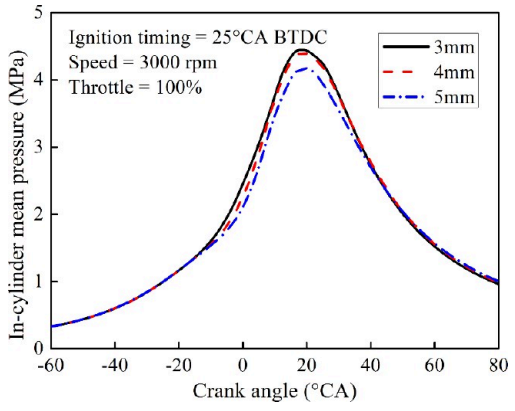

Figure 1. In-cylinder mean pressure grid independence verification.

compares the chamber pressures under different grid sizes. Among them, the difference in 3 and 4 mm chamber pressure curves is slight, and the maximum relative error is within 5%. Four millimeters is chosen as the basis grid size taking into account computation accuracy and time cost. So, the interior of the cylinder is permanently encrypted at two levels, and the grid size is 1 mm after encryption; the inlet cone angle is permanently encrypted at three levels to improve the ability to capture the development of inlet turbulence, and the grid size is 0.5 mm after encryption. The injection nozzle is encrypted at three levels, and the grid size is 0.5 mm after encryption; two levels of encryption are applied to the spark plug, resulting in mesh sizes of 0.125 and 0.25 mm. In order to accurately calculate turbulent motion and the combustion development process, adaptive mesh refinement (AMR) is selected to encrypt the velocity and temperature field. The cylinder and the air intake area are encrypted with a three-level permanent AMR. When the speed gradient difference between adjacent grids exceeds 1 m/s, the self-adaptive encryption is carried out, and the grid size is 0.5 mm after encryption. During the combustion period from 30 °CA before top dead center (BTDC) to 120 °CA after top dead center (ATDC), the cylinder area is encrypted with three levels of permanent AMR. When the temperature gradient difference between adjacent grids exceeds 2.5 K, the self-adaptive encryption is carried out, and the size of the encrypted grid is 0.5 mm. Figure 2 at 25 °CA BTDC depicts the CONVERGE simulation model's computational domain grid.

This simulation makes use of the RNG K-ε turbulence model that provides an excellent accurate prediction for the flow field, to precisely forecast the flow field distribution.[26,27] The wall-function model is used in this simulation, which can accurately capture wall heat loss.[28] The SAGE model is applied by the combustion model because it is more effective than the empirical model at predicting detonation, self-ignition, and emissions.[29] The SAGE model estimates combustion directly based on a precise reaction mechanism, allowing CO and HC emissions to be estimated. Furthermore, the extended Zel'dovich model[30] and the Hiroyasu model[31] can predict NO_X and soot emissions, respectively. Table 2 shows the choice of the 3d simulation model. On the basis of 124 reactions and 41 species, the primary reference fuel (PRF) reaction model is chosen. The model maintains precise ignition delay predictions while emphasizing laminar flame velocities and significant species evolution.[32] The 3d simulation boundary conditions are listed in Table 3.

2.2. Experiment Description and Model Validation. In this experiment, Sinopec 92 # gasoline is selected as the bench test fuel, and the injection timing and the injection pulse width are 460 °CA BTDC and 7.23 ms, respectively. PowerLink FC2000 internal combustion engine measurement and control system are used in engine bench tests. The name of the testing equipment is shown in Table 4. Engine speed, throttle opening, and other variables were controlled by the control cabinet control. Temperature sensors, intake pressure sensors, speed sensors, and throttle position sensors can monitor the parameters of the engine running in real time and constantly give feedback and control the engine. The KiBox Type, 8920 combustion analysis instrument by Kistler Instrumente AG, is used to measure the in-cylinder pressure, pressure rise rate, and heat release rate. The schematic for the original engine bench test system is shown in Figure 3. The bench test is performed on the original engine with a speed interval of 500 r·min^{-1} from 2000 to 6000 r·min^{-1}, and 3000 r·min^{-1} with a throttle opening of 100% is selected to perform the simulation. Figure 4 displays the chamber pressure and heat release rate curves from the bench test and simulation. The peak values of chamber pressure and heat release rates in test and 1d and 3d simulations are (4.27 MPa, 13.16 J/°CA), (4.3 MPa, 13.28 J/°CA), and (4.25 MPa, 13.4 J/°CA). The model has been thoroughly verified, as the greatest relative errors are less than 5%.

2.3. Simulation Method for Ultrasonic-Fed the Chamber. This paper tentatively proposes a multifield coupled numerical simulation method, which embeds ultrasonic physics into the chamber. The ultrasonic wave can be typically generated by the sound source surface's high-frequency sine wave movement, as shown in eq 1. Therefore, the ultrasonic simulation can be approximately realized using CFD software's

https://doi.org/10.1021/acsomega.3c05415
ACS Omega 2023, 8, 36418−36434

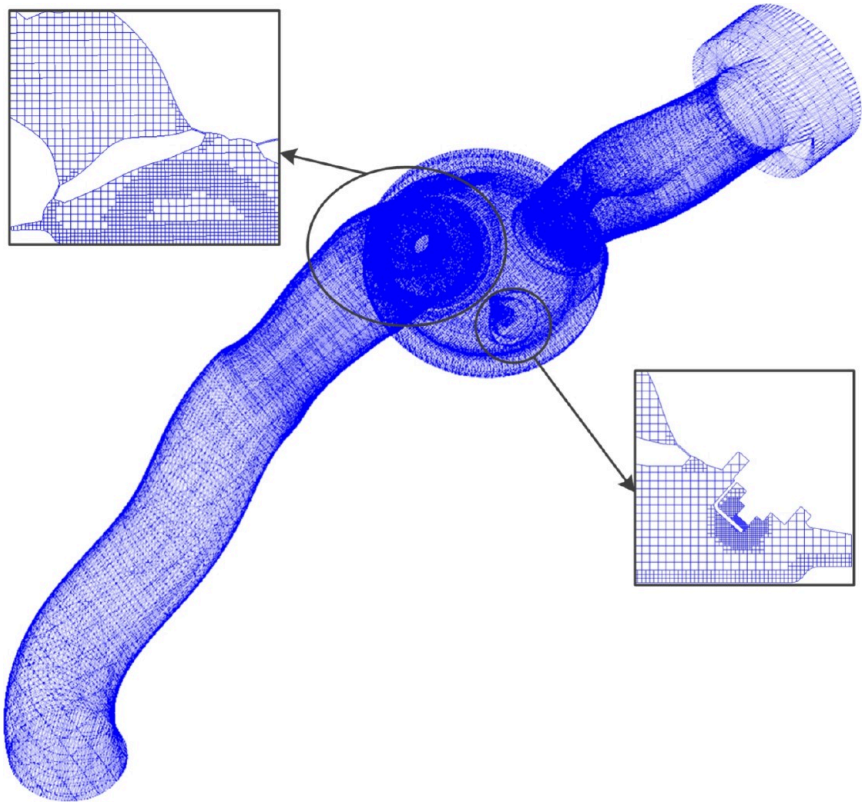

Figure 2. Computational domain mesh at 25 °CA BTDC.

Table 2. Choice of 3d Simulation Model

description	model
soot formation	Hiroyasu model
NO_X formation	extended Zel'dovich mechanism
turbulence	RNG k-ε model
combustion	SAGE model
ignition	spark-energy deposition model

Table 3. Summary of 3d Simulation Boundary Conditions

parameter	type	value
inlet/outlet pressure	inflow	GT-Power
inlet/outlet temperature	outflow	GT-Power
cylinder wall temperature	fixed wall	520 K
piston wall temperature	moving wall	590 K
spark-plug wall temperature	fixed wall	550 K
spark-electrode wall temperature	fixed wall	950 K
top of exhaust valve temperature	moving wall	650 K
bottom of exhaust valve temperature	moving wall	650 K
top of intake valve temperature	moving wall	350 K
bottom of intake valve temperature	moving wall	350 K
inlet valve cone angle temperature	moving wall	350 K
intake port temperature	fixed wall	330 K
exhaust port temperature	fixed wall	640 K
ignition timing		25 °CA BTDC

dynamic grid function.[33−35] The ultrasonic simulation is sufficiently realized using the CONVERGE software's dynamic grid function. Additionally, the data points (t_{CA}, y) can be acquired by MATLAB and the relational expressions are provided in eqs 2 and 3. The time t is transformed to the crankshaft angle t_{CA} that corresponds to 3000 r·min^{-1}. The

Table 4. Summary of Experimental Equipment

name	type	name	type
engine measurement and control instrument	FC2010	data acquisition instrument	FC2020
dynamometer	GW100	fuel consumption meter	FC2210Z
throttle position sensor	ETS20X	combustion analyzer	type 2893A
throttle actuator	FC2310	intake pressure sensor	EHM100

corresponding relationship at different frequencies after the transformation is shown in Table 5. In the CONVERGE software, feeding ultrasonics can be realized by setting the ultrasonic boundary to move according to the change law of (t_{CA}, y) coordinates.

$$y = A\sin(2\pi ft) \tag{1}$$

$$t_{CA} = \frac{t}{T}T_{CA} + a \tag{2}$$

$$T_{CA} = \frac{n}{60}2\pi\frac{1}{f} = \frac{\pi n}{30f} \tag{3}$$

In this equation, A represents the amplitude, t represents the time, y represents the variation in time t, n represents the engine speed, f represents the frequency, T_{CA} represents the crankshaft angle period, T represents the period, t_{CA} represents the crankshaft angle, and a represents the crankshaft angle at the initial phase of the ultrasonic feed.

Intentionally incorporated to the original engine's geometric model is the structural feature of the ultrasonic surface, whose axis runs through the middle of the spark plug electrode gap. The

https://doi.org/10.1021/acsomega.3c05415
ACS Omega 2023, 8, 36418−36434

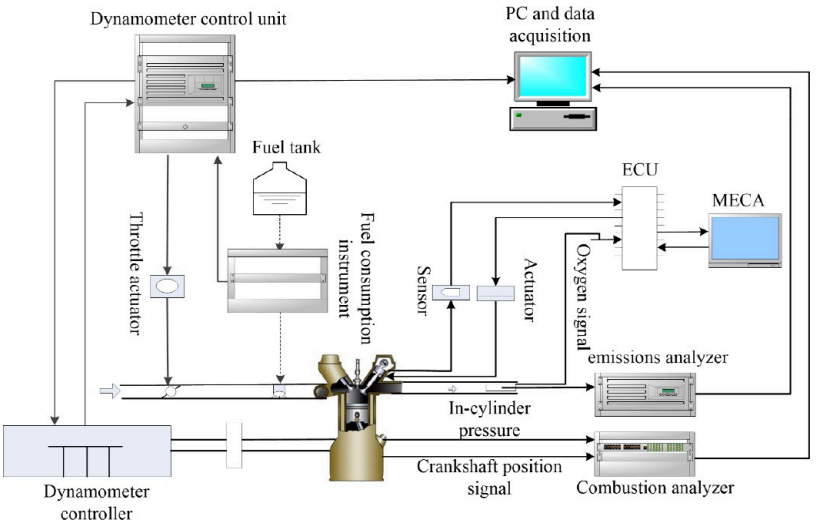

Figure 3. Experimental equipment schematic.

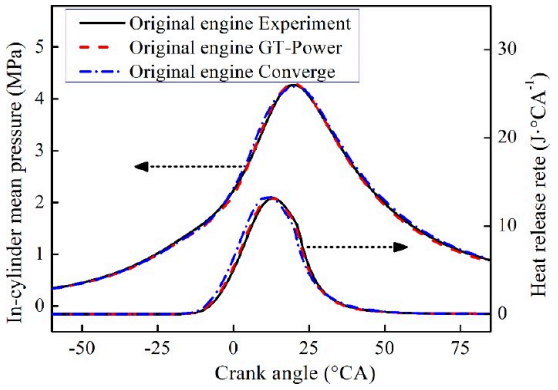

Figure 4. Comparison of chamber pressure and heat release rate.

Table 5. Corresponding Relationship at Different Frequencies

speed (r·min^{-1})	period (T_{CA},°CA)	period (T, s)	frequency (kHz)
3000	0.9	5×10^{-5}	20
3000	0.6	3.3×10^{-5}	30
3000	0.45	2.5×10^{-5}	40
3000	0.36	2×10^{-5}	50

geometric diameter of the ultrasonic surface is 10 mm, as shown in Figure 5. Mach CFL number is a calculated time step based on sound speed. In order to fully capture ultrasonic high-frequency pressure waves, it is set to 3.5, and at least 25 sampling points are output in each ultrasonic vibration cycle time. Because this research is the first application of CONVERGE software to realize the coupling of the sound field and combustion field, it is necessary to consider the division of the sound field grid. The

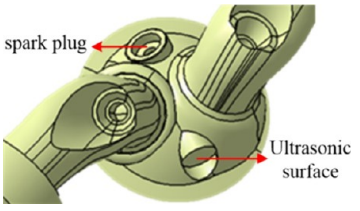

Figure 5. Ultrasonic surface.

current work does not take into account the superposition of the impedance and acoustic reflection variables for the sake of simplification. With the aim to faithfully record the transmission of the ultrasonic high-frequency radiation pressure wave, it is necessary to ensure that at least 5 grids are arranged within a wavelength. Wavelength calculation is shown in eqs 4 and 5. Sound velocity is affected by changes in the density and pressure of the cylinder, and its sound velocity is also a transient value, as shown in Figure 6. Taking 50 kHz feed-in at 134 °CA BTDC−

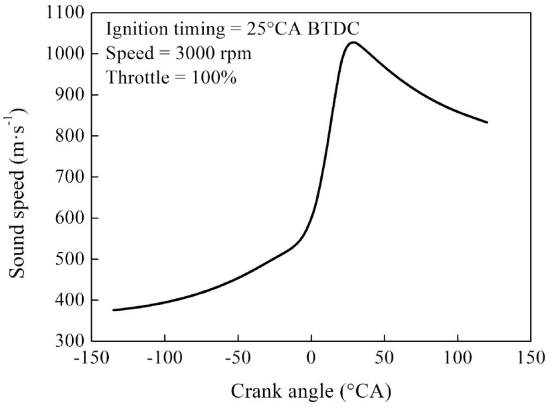

Figure 6. Changes in in-cylinder sound speed.

120 °CA ATDC as an example, the mesh encryption level of the ultrasonic domain is correctly calculated. At 134 °CA BTDC, the minimum sound speed is 376 m/s and the corresponding wavelength is 0.00752 m. At 29 °CA ATDC, the maximum sound speed is 1028 m/s and the corresponding wavelength is 0.02056 m. In the CONVERGE numerical simulation model, the basic grid is 0.004m, and the size of the grid after encryption is 0.001 m. The wavelength is 7.52 − 20.56 times the size of the encrypted grid. So, there are 7.52− 20.56 grids in one wavelength, which is much larger than 5 computational grids and meets the computing requirements.

$$\lambda = \frac{c}{f} \tag{4}$$

https://doi.org/10.1021/acsomega.3c05415
ACS Omega 2023, 8, 36418−36434

Table 6. Amplitude Corresponding to Each Simulation Scheme

case	SA1	SA2	SA3	SA4	SA5	SA6
amplitude	60 μm	100 μm	140 μm	180 μm	220 μm	260 μm

$$c = \sqrt{\frac{\gamma P}{\rho}} \tag{5}$$

In this equation, c represents the speed of sound, λ represents the heat capacity ratio, P represents the pressure, and ρ represents the density.

3. RESULTS AND DISCUSSION

3.1. Effect of Constant Frequency Variable Amplitude Ultrasonic on Combustion Performance. During ultrasonic horn operation, its driving frequency is usually 20−30 kHz. When the mechanical vibration caused by the piezoelectric element is transmitted to the rod's tip, its displacement can reach up to several 100s μm.[33,36] By altering the energy converter's input power, the displacement of the horn may be accurately altered. Previous research has demonstrated that the influence of the ultrasonic-fed time on the combustion increases with time.[25] So, in this study, the ultrasonic-fed time is set as the inlet valve closing to the exhaust valve opening (134 °CA BTDC to 120 °CA ATDC (14.1 ms)), frequency is selected as 20 kHz, and the amplitude is selected as 30−300 μm, to adequately explore the influence of constant frequency variable amplitude ultrasonic on the combustion performance in the cylinder. In order to facilitate analysis, six representative groups of simulation results are selected for analysis within the amplitude range of 30−300 μm with 40 μm intervals, as shown in Table 6.

3.1.1. Effect of Constant Frequency Variable Amplitude Ultrasonic on Flow Field Distributions. The high-frequency sine wave movement of the source surface generates ultrasonic waves. With the increase of the input power of the energy converter, its frequency remains unchanged and its amplitude increases relatively. The stronger the ultrasonic energy is, the greater the potential is the impact on the flow field, especially the impact on the ignition timing and TDC. Therefore, the in-cylinder flow field is typically analyzed at 25 °CA BTDC and 0 °CA TDC. Table 7 shows the in-cylinder spatial distribution of the velocity field, equivalence ratio (Φ), and TKE. For the velocity field, the greater the amplitude, the greater the influence on the in-cylinder velocity. In particular, when the amplitude reaches 100 μm, the velocity of the spark plug attachment begins to increase, and then with the amplitude increase, the velocity field near the spark plug increases significantly. However, the increase in amplitude does not have a great influence on the distribution of Φ. For the TKE, the greater the amplitude, the stronger the TKE level. Specifically, TKE increases progressively with increasing amplitude at 25 and 0 °CA TDC as compared to scheme No, as seen in Figure 7. When the amplitude reaches 260 μm, the TKE increases by 46.6% at 25 °CA BTDC and 93.8% at 0 °CA TDC. The pressure waves generated by ultrasonic vibration can cause significant interference to the flow field, and as the amplitude increases, the TKE significantly increases. A higher TKE distribution will favor the progression of turbulence and initial flame.[37,38]

To further quantify the consequence of ultrasonic on in-cylinder flow characteristics under different amplitudes, the changes of turbulent velocity and turbulent dissipation rate in the chamber are analyzed at the 25 °CA BTDC in Figure 8. Turbulent velocity (u') and turbulent dissipation rate (ε) are determined as shown in eqs 6 and 7. The figure shows that the ultrasonic feeding enhances the turbulent flow in the chamber. With the increase of amplitude, the in-cylinder turbulent velocity and turbulent dissipation rate are significantly improved, thus improving the propagation velocity of the initial flame and improving the combustion efficiency. The increase in the turbulence velocity and turbulence dissipation rate is the result of ultrasonic mechanical vibration, and high-frequency harmonic vibration is clearly beneficial for the full development of turbulent motion in the combustion chamber. Also, turbulent motion is further enhanced with the increase of amplitude.

$$u' = \sqrt{\frac{2}{3}k} \tag{6}$$

$$\varepsilon = \frac{C_\mu^{3/4} k^{3/2}}{le} \tag{7}$$

In this equation, k represents the TKE, C_μ represents the turbulence model constant, and le represents the length scale.

3.1.2. Effect of Constant Frequency Variable Amplitude Ultrasonic on Combustion Behavior. Figure 9 depicts the propagation of flame at 2000 K[39] at different crankshaft angles. After ignition, when the crankshaft angle is rotated at 15 °CA, the fire core forms at different amplitudes near the spark plug. At this time (10 °CA BTDC), there is a significant difference in the size of the fire core. With the increase of the amplitude, the larger the fire core. As combustion continues, there are significant differences in the flame propagation process in the combustion chamber. Due to the lack of ultrasonic feed, the turbulence intensity near the spark plug is lower in scheme No, so the flame propagation speed is slower in this scheme. From the simulation results of the SA1−SA6 scheme, it can be seen that the ultrasonic-fed turbulence makes the turbulence intensity near the spark plug higher, and this turbulence intensity increases with the increase of amplitude and finally improves the flame propagation speed in the chamber as a whole.

To further study the effect of the amplitude on flame propagation, the burned volume rate in the combustion chamber is quantitatively analyzed. The space volume enclosed by the isosurface at 2000 K is defined as the burned volume, as shown in Figure 10. As shown in the graph, the change in the burned volume rate increases initially and then declines from the ignition moment. The trend of its first increase is positively correlated with the increase of the amplitude, and the peak value of the change rate of burned volume of the SA6 scheme with the largest amplitude appears first. The subsequent decreasing trend is negatively correlated with the amplitude increase, and the change rate of burned volume for the SA6 scheme with the largest amplitude decreases first and then the fastest. The peak value of the change of burned volume rate appears earliest, indicating that the flame propagates faster under this amplitude. The subsequent decrease in the burned volume rate is due to the quenching phenomenon when the flame front hits the wall, and with the increase in the amplitude, the decrease in the burned volume rate gradually increases. This quenching phenomenon is one of the leading causes of HC formation.

Based on the above analysis, it is necessary to accurately analyze the internal mechanism of how ultrasonic-fed fuel affects

https://doi.org/10.1021/acsomega.3c05415
ACS Omega 2023, 8, 36418−36434

Table 7. Velocity Field and TKE Distribution

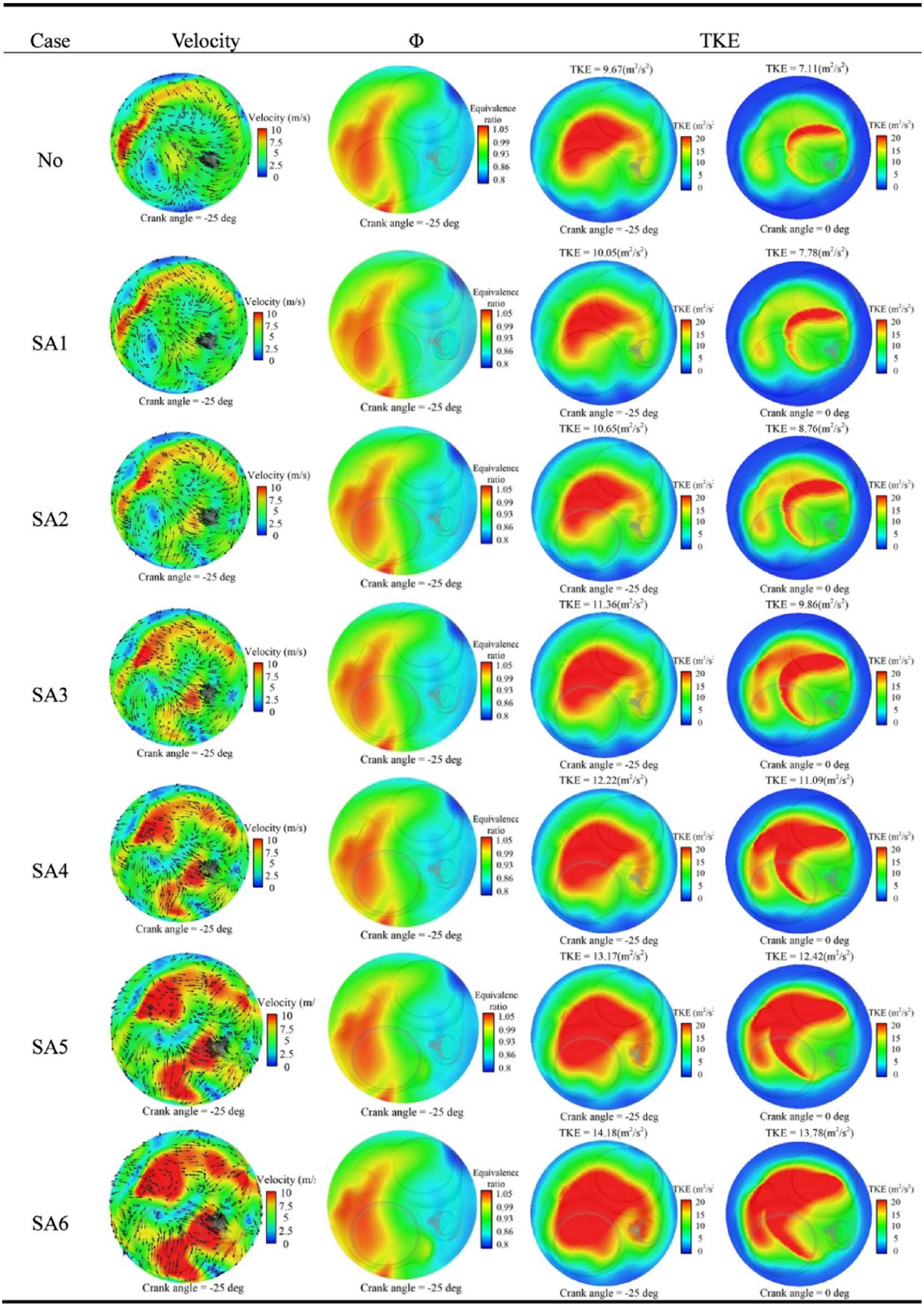

https://doi.org/10.1021/acsomega.3c05415
ACS Omega 2023, 8, 36418−36434

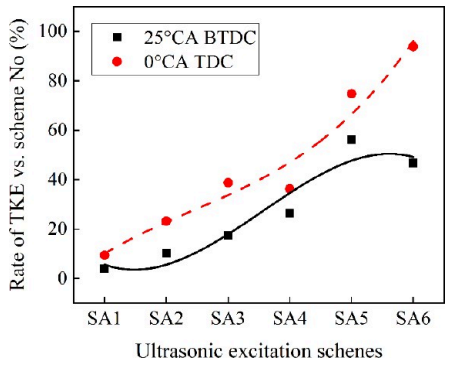

Figure 7. Variations of the TKE rates vs scheme No.

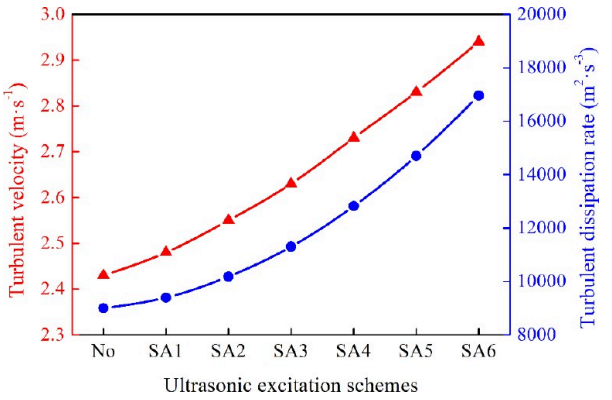

Figure 8. Changes in in-cylinder turbulence velocity and turbulence dissipation rate at 25 °CA BTDC.

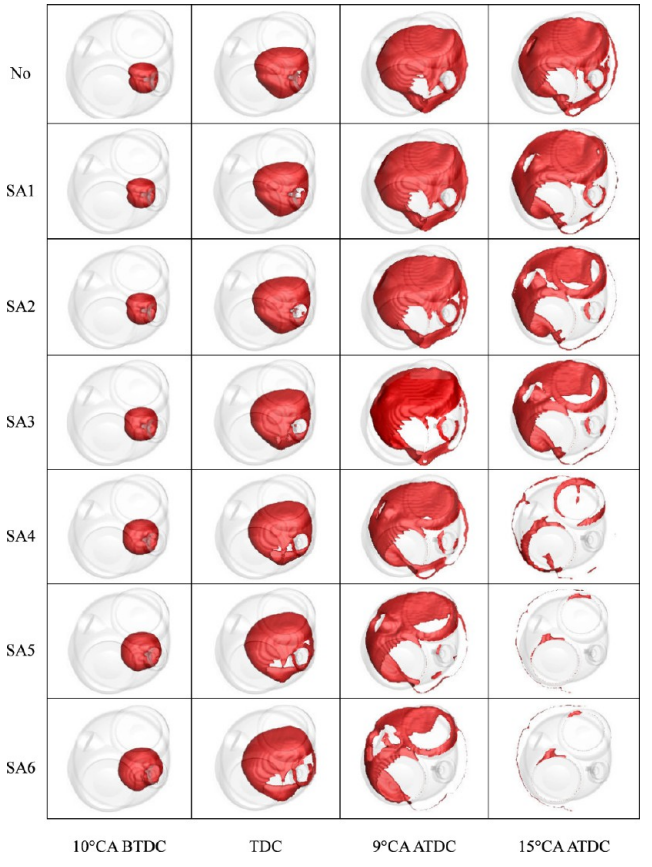

Figure 9. Flame propagation contour at various crankshaft angles.

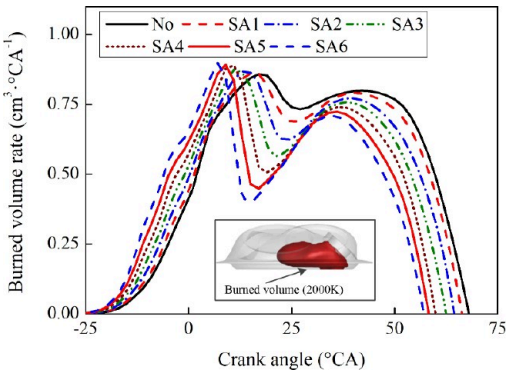

Figure 10. Changes in burned volume rate.

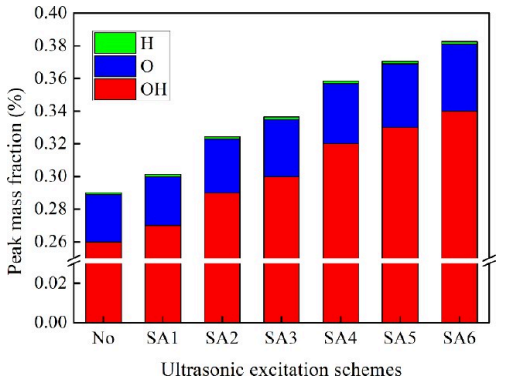

Figure 11. Total peak mass fraction of the OH, O, and H radicals.

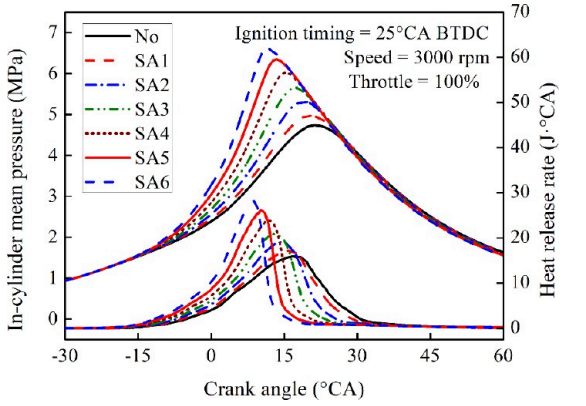

Figure 12. Variations of combustion pressure and heat release rate.

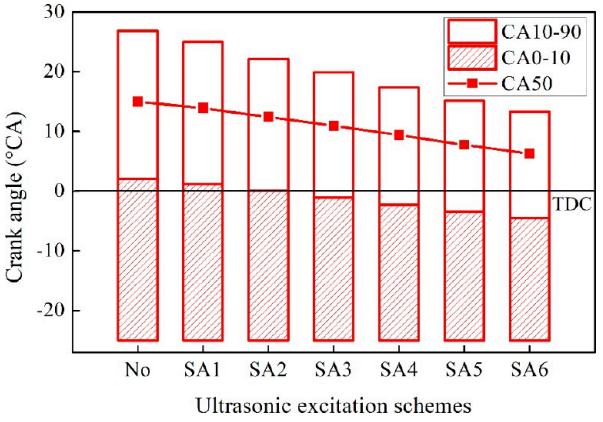

Figure 13. Variations of in-cylinder CA10, CA50, and CA90.

https://doi.org/10.1021/acsomega.3c05415
ACS Omega 2023, 8, 36418−36434

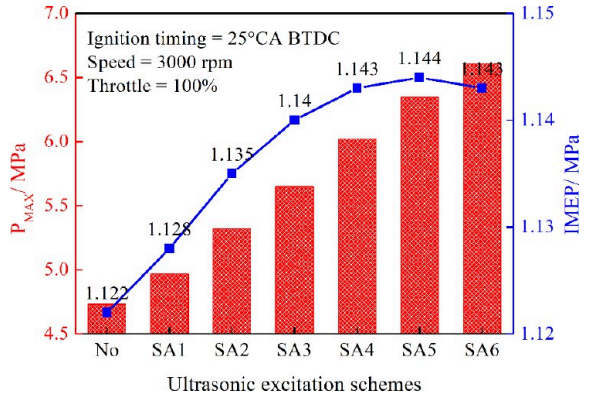

Figure 14. Variations of in-cylinder P_{MAX} and IMEP.

flame development. The chemical reaction mechanism of PRF showed that the concentration of OH, O, and H active radicals has a very severe effect on the combustion reaction. In Figure 11, each scheme's peak mass fraction of the OH, O, and H radicals is represented by a stacked column. Based on the figure, it is clear that ultrasonics can increase the concentration of three kinds of active free radicals. Also, as the amplitude increases, the δ increases. Under ultrasonic, the branched-chain reaction OH + $H_2 \Leftrightarrow H + H_2O$ and $H + O_2 \Leftrightarrow O + OH$ become extremely active, and more free radicals are rapidly generated. With the increase of amplitude, this process is continuously accelerated, thus promoting the development of the flame and improving the combustion efficiency.

Figure 12 shows the changes in the in-cylinder pressure and heat release rate at different amplitudes. It can be seen from the figure that with the increase of amplitude, the slope of pressure and heat release rate gradually increases. Among them, the SA6 scheme with the largest amplitude has the most significant slope of in-cylinder pressure and heat release rate curve, sufficiently indicating that the SA6 scheme has the fastest combustion rate, whose peak values are 6.6 MPa and 28.3 J/°CA, respectively. Compared with scheme No, the in-cylinder P_{MAX} of the SA6 scheme increased by 1.9 MPa, and the peak heat release rate increased by 12.4 J/°CA. For different ultrasonic amplitudes, ultrasonic-fed improves the in-cylinder TKE, increasing the in-cylinder pressure and heat release rate. Figure 13 compares the changes in the combustion phase under different amplitudes, including ignition time (CA0−10), main combustion period (CA10−90), and combustion center of gravity (CA50). As we can see from the figure, the effect of ultrasonics makes the combustion phase shorten, and with the increase of amplitude, the combustion phase gradually shortens more obviously. This is mainly because the ultrasonic feeding improves the turbulence intensity in the cylinder, promotes the formation of active free radicals, and ultimately improves the reaction rate of branched radicals, resulting in the shortening of the combustion phase.

Figure 14 shows the changes of in-cylinder P_{MAX} and the indicated mean effective pressure (IMEP) under different amplitudes. With the increase of amplitude, P_{MAX} increases and IMEP also increases. Among them, IMEP of SA1−SA6 increased by 0.5, 1.2, 1.6, 1.9, 2.0, and 1.9%, respectively. This indicates that ultrasonic-fed does obviously improve combustion efficiency. Simultaneously, the amplitude increase cannot significantly improve the combustion efficiency. The change rate of IMEP reaches the maximum when the amplitude is 220 μm, and the increase of IMEP is very limited in this condition.

3.1.3. Effect of Constant Frequency Variable Amplitude Ultrasonic on Emission Formation. In order to describe the effects of amplitude on the generation of four conventional emissions, Figure 15 and Figure 17 show the rates of NO_X, HC, CO, and soot mass in the combustion chamber at 120 °CA ATDC. As we can see from Figure 15a, with the amplitude increase, the temperature curve rises more obviously. As shown in Figure 15b, more NO_X emissions are formatted with an increase in the amplitude increase. Among them, the NO_X increased by 32.4% in the SA6 scheme. The formation of NO_X is mainly affected by in-cylinder combustion temperature, oxygen concentration, and duration of high temperature.[40] The ultrasonic-fed gas makes the combustion chamber temperature rise, which promotes NO_X formation to a certain extent, and the NO_X formation increases with the increase of amplitude. HC formation belongs to the component of unburned fuel in the combustion chamber; therefore, IC_8H_{18} is used to represent HC formation, as shown in Figure 16. At the frequency of 20 kHz, HC formation of all amplitudes is concentrated on one side of the sound source surface. It can be seen that the addition of the sound source surface leads to the appearance of an irregular shape of the combustion chamber, especially the appearance of the narrow gap in the combustion chamber directly deteriorates the combustion environment of the working medium near the wall surface, leading to the HC surge. On the one hand, the ultrasonic-fed accelerates the flame propagation to a certain extent and simultaneously accelerates the quenching phenomenon when the flame front hits the wall. On the other hand, ultrasonic-fed will produce a large number of cyclic fluctuations, resulting in high strain in the flame front, which will lead to local

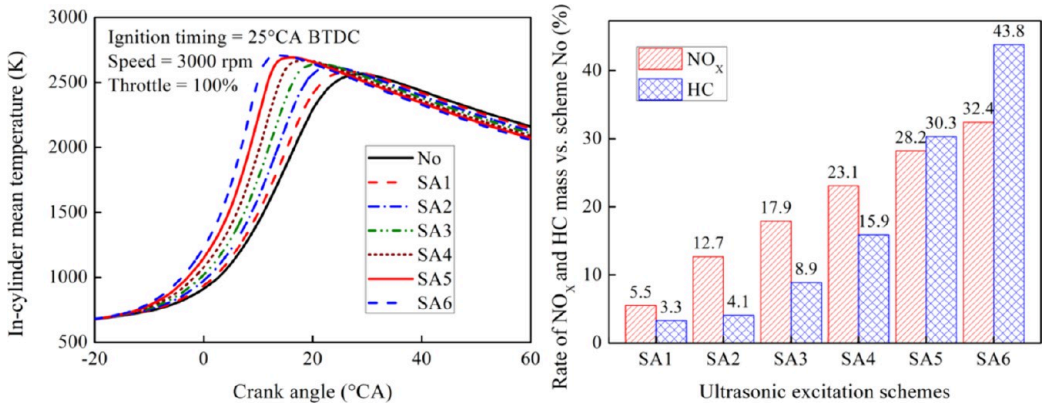

Figure 15. In-cylinder temperature and the variations of the NO_X and HC mass rates vs scheme No.

https://doi.org/10.1021/acsomega.3c05415
ACS Omega 2023, 8, 36418−36434

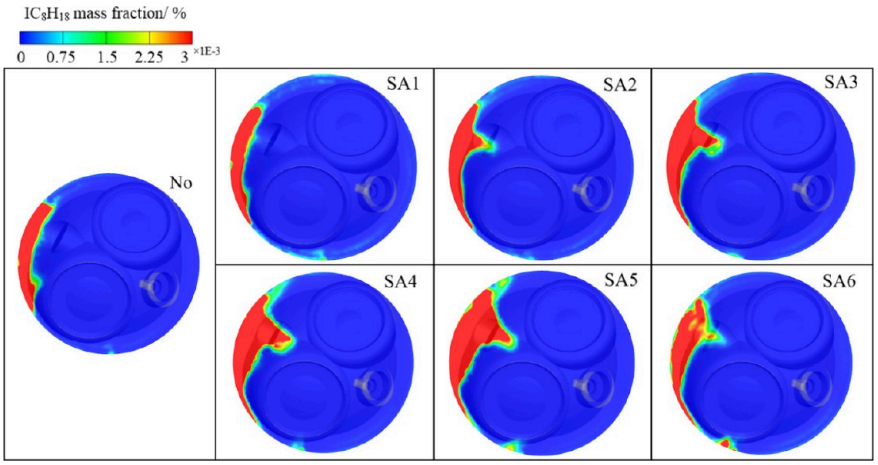

Figure 16. Distribution of IC_8H_{18} at 120 °CA ATDC.

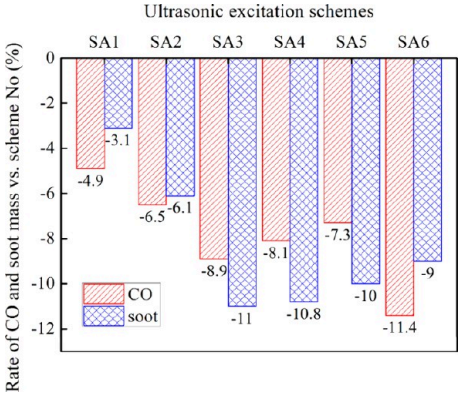

Figure 17. Variations of the CO and soot mass rates at 120 °CA ATDC.

flame extinction, and this phenomenon becomes more severe with the increase of amplitude. These are the main reasons for the increase in HC emissions, among which SA6 increased HC by 43.8%.

Concentrations of OH, O, and H active radicals and combustion temperature in the combustion chamber are the main reasons affecting CO formation.[41] With the ultrasonic action and the increase of amplitude, a large number of active free radicals are generated in the combustion chamber (as shown in Figure 11) and a high combustion temperature (as shown in Figure 15a), which promoted the oxidation of CO through reaction pathways of CO + OH ⇔ CO_2 + H and O + CO + M ⇔ CO_2 + M. Therefore, the formation of CO in SA1−SA6 schemes decreased significantly. Figure 18 shows the spatial distribution of CO in the combustion chamber at 120 °CA ATDC, and its formation is mainly concentrated on the side of the sound source surface. It can be seen that the change in combustion chamber shape caused by the sound source surface is still one factor leading to incomplete fuel combustion. Among them, the level of CO decreased by 11.4% in the SA6 scheme. The addition of ultrasonics enhances the turbulence intensity in the combustion chamber and forms high-frequency cyclic fluctuations for the fuel. The turbulence intensity and cyclic fluctuations also gradually increase with an increase of amplitude. Strong cyclic fluctuations harm HC emissions, but at the same time, they also hinder soot formation and accelerate

Table 8. Frequency Corresponding to Each Simulation Scheme

case	SB1	SB2	SB3	SB4
frequency	20 kHz	30 kHz	40 kHz	50 kHz

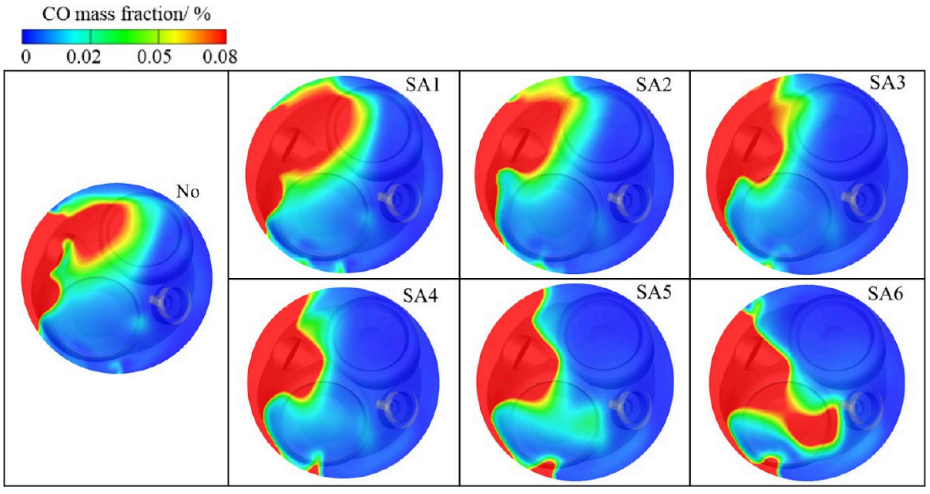

Figure 18. Distribution of CO at 120 °CA ATDC.

https://doi.org/10.1021/acsomega.3c05415
ACS Omega 2023, 8, 36418−36434

Table 9. Velocity field and TKE Distribution

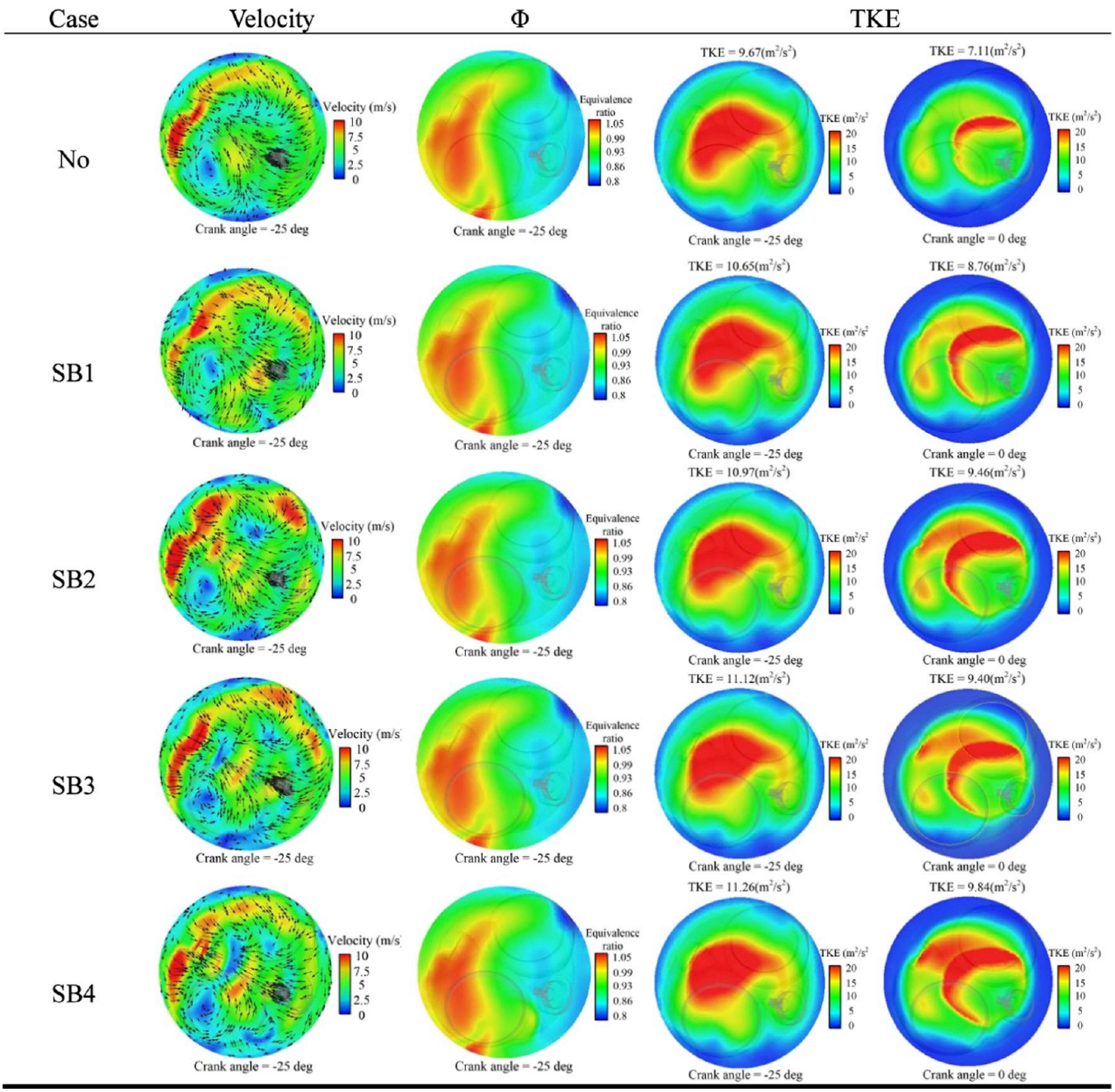

the soot's oxidation process. Among them, the SA3 scheme has the largest soot reduction, up to 11%.

3.2. Effect of Variable Frequency Constant Amplitude Ultrasonic on Combustion Performance. The frequency of the energy converter is inversely proportional to the amplitude. The greater the frequency, the smaller the amplitude that the rod tip can reach. Considering the selected frequency, the amplitude that the energy converter can achieve, so the amplitude is set to 100 μm. The frequency is selected as a 20−50 kHz cavitation-prone interval. In this study, the ultrasonic-fed time is set as the inlet valve closing to exhaust valve opening (134 °CA BTDC to 120 °CA ATDC (14.1 ms)),[25] and the simulation results of four groups of different frequencies are analyzed within the frequency range of 20−50 kHz at an interval of 10 kHz, as shown in Table 8. The influence mechanism of variable frequency constant amplitude ultrasonics is investigated on the ignition, combustion, and emissions.

3.2.1. Effect of Variable Frequency Constant Amplitude Ultrasonic on Flow Field Distributions. Under the same amplitude, the higher the ultrasonic frequency, the stronger the external output energy will be and the greater the influence on the combustion chamber flow field, especially at 25 and 0 °CA TDC. Table 9 objectively compares different frequency simulation results with scheme No in the velocity field, Φ, and TKE. For the velocity field, the difference in velocity field between different frequencies is obvious. When the frequency reaches 20 kHz, a strong flow field is generated near the spark plug at 25 °CA BTDC; when the frequency reaches 30 kHz, the

https://doi.org/10.1021/acsomega.3c05415
ACS Omega 2023, 8, 36418−36434

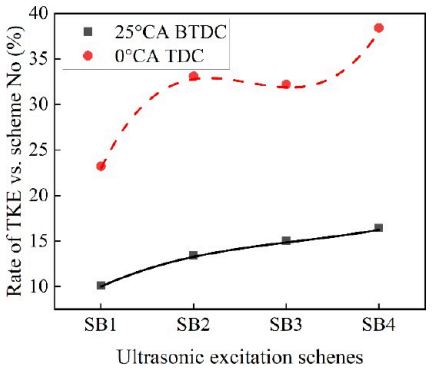

Figure 19. Variations of the TKE rates vs scheme No.

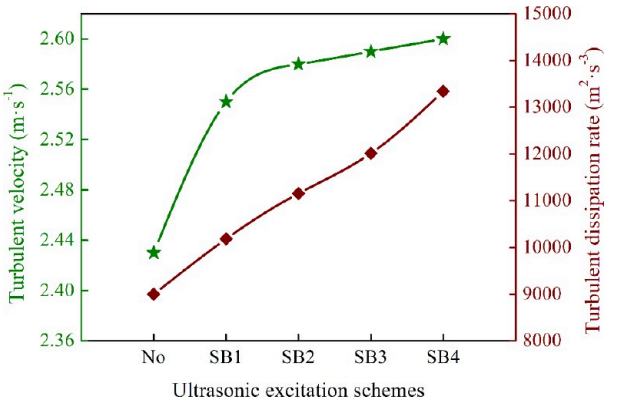

Figure 20. Variations of in-cylinder turbulence velocity and turbulence dissipation rate at 25 °CA BTDC.

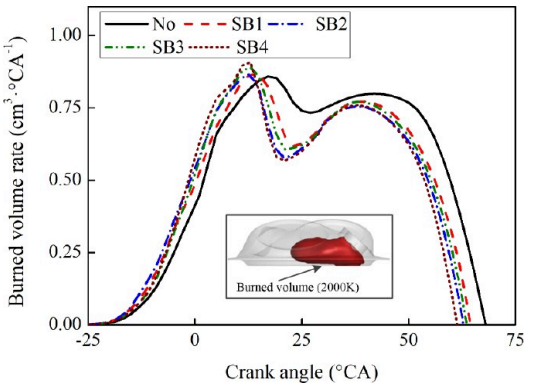

Figure 22. Variations of burned volume rate.

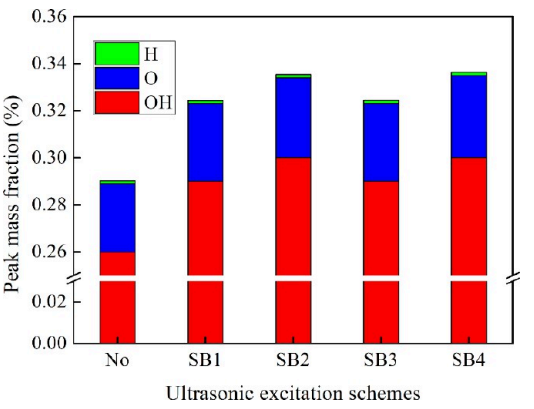

Figure 23. Total peak mass fraction of the OH, O, and H radicals.

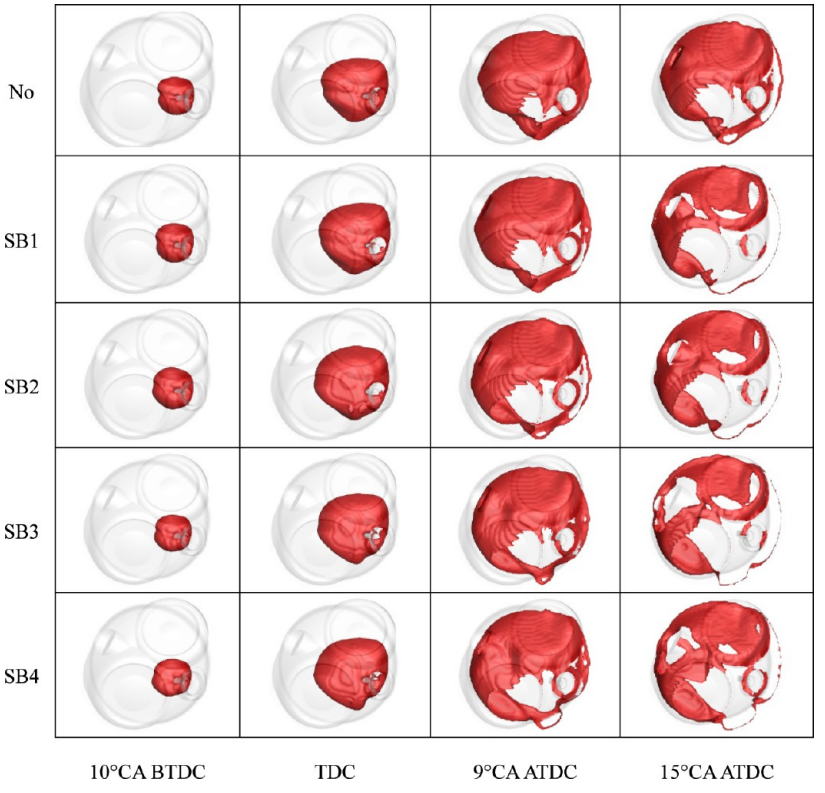

Figure 21. Flame propagation contour at various crankshaft angles.

https://doi.org/10.1021/acsomega.3c05415
ACS Omega 2023, 8, 36418−36434

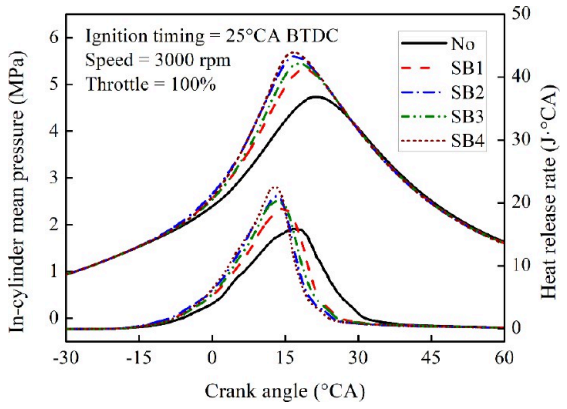

Figure 24. Variations of in-cylinder pressure and heat release rate.

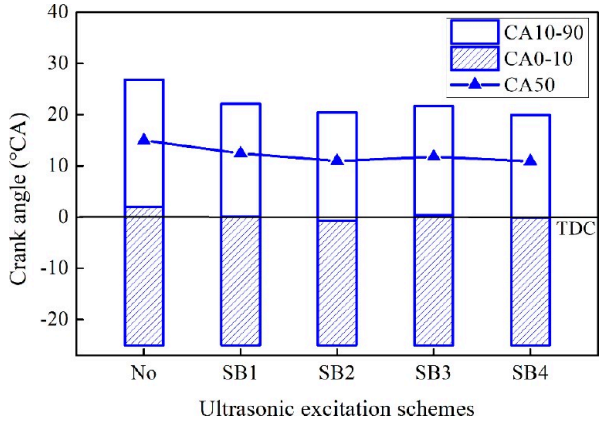

Figure 25. Variations of in-cylinder CA10, CA50, and CA90.

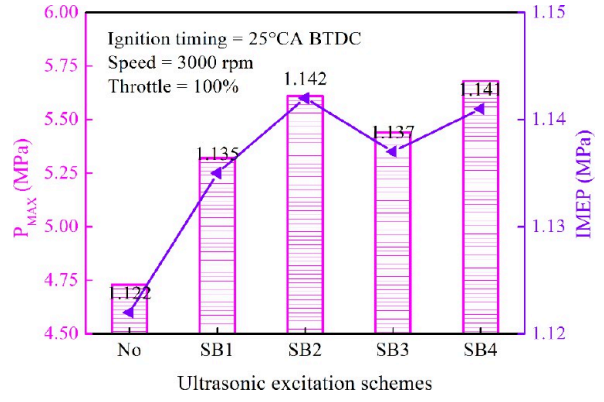

Figure 26. Variations of in-cylinder P_{MAX} and IMEP.

transmission process of the sound wave can be observed in the velocity field, and the propagation of the sound wave becomes more intense with the increase of frequency. However, at the frequency of 20−50 kHz, the continuous input of ultrasonic energy has no obvious influence on the distribution of fuel. For TKE, as the frequency increases, the in-cylinder TKE becomes stronger, as shown in Figure 19. Among them, when the frequency reaches 50 kHz, TKE increases the most at 25 and 0 °CA TDC, reaching 16.4 and 38.4%, respectively. This is because the high-frequency radiation pressure generated by ultrasonics can disrupt the flow field in the combustion chamber, and this disturbance will increase with increasing frequency. At 25 to 0 °CA TDC, a higher TKE has a favorable influence on the growth of the initial flame.[33,37]

In order to further quantify the influence of ultrasonic on in-cylinder flow characteristics at different frequencies, Figure 20 analyzes the changes in turbulent velocity and turbulent dissipation rate in the combustion chamber at 25 °CA BTDC. The calculation methods are shown in eqs 6 and 7. As we can see from the figure, the turbulence dissipation rate increases with an increase in frequency, presenting a linear trend. The turbulent velocity increases with the increase of frequency but does not increase significantly between 20 and 50 kHz. Ultrasonic-fed improves the TKE level in the combustion chamber and increases the initial flame propagation velocity and combustion chemical reaction rate.

3.2.2. Effect of Variable Frequency Constant Amplitude Ultrasonic on Combustion Behavior. Figure 21 shows the distribution of flame propagation in the chamber at different frequencies. After ignition, when the crankshaft angle is rotated at 15 °CA, the fire core near the spark plug has been formed at different frequencies with little difference. However, when the crankshaft angle is rotated 9 °CA at TDC, the flame propagation significantly differs. With the increase of frequency, the propagation speed of the flame increases obviously. As can be seen from Figure 19, the increase in frequency leads to a higher TKE near the spark plug, thus increasing the flame propagation velocity in the combustion chamber. In order to further study the influence of ultrasonics on flame propagation velocity at different frequencies, the burned volume in the combustion chamber at any crankshaft position is quantitatively analyzed, as shown in Figure 22. It can be seen from the figure from the ignition moment, the change of burned volume increases first and then decreases. The first increased volume means that the flame propagation speed is accelerated. On the one hand, the quenching phenomenon occurred when the flame front hit the wall, and on the other hand, the local strain of the flame front caused by the high-frequency vibration in the combustion chamber led to flame extinction. These two factors are the main causes of HC formation. When the frequency reaches 40−50 kHz, the burned volume rate increases, and when it reaches the earliest peak position, there is an instantaneous decline near 9 °CA ATDC because the excessive frequency negatively impacts flame propagation.

Based on the above, how different ultrasonic frequencies affect the internal mechanism of the flame is analyzed. The δ is shown by a stacked column in Figure 23. According to the PRF reaction mechanism, the concentration of OH, O, and H active free radicals significantly affects the combustion reaction. As we can see from the figure, the increase in frequency increases the δ to some extent, but it is not in direct proportion to the increase in frequency. Among them, the δ at 30 kHz is significantly less than at 20 kHz. The order of the δ is SB4 > SB2 > SB3 > SB1 > No. Under ultrasonic excitation, the rate of branched chain reaction containing OH, O, and H free radicals is accelerated. Then more free radicals are generated, which accelerated with the increase in frequency, thus promoting flame development and improving combustion efficiency.

Figure 24 shows the changes in in-cylinder pressure and heat release rate with the crankshaft angle at different frequencies. As we can see from the figure, with the increase in frequency, the slope of the pressure and heat release rate gradually increases. The SB4 scheme has the highest slope of pressure and heat release rate, indicating that SB4 has the fastest combustion speed, and its peak values are 5.7 MPa and 22.5 J/°CA, respectively. Compared with scheme No, the in-cylinder P_{MAX} increases by 1 MPa, and the peak heat release rate increases by

https://doi.org/10.1021/acsomega.3c05415
ACS Omega 2023, 8, 36418−36434

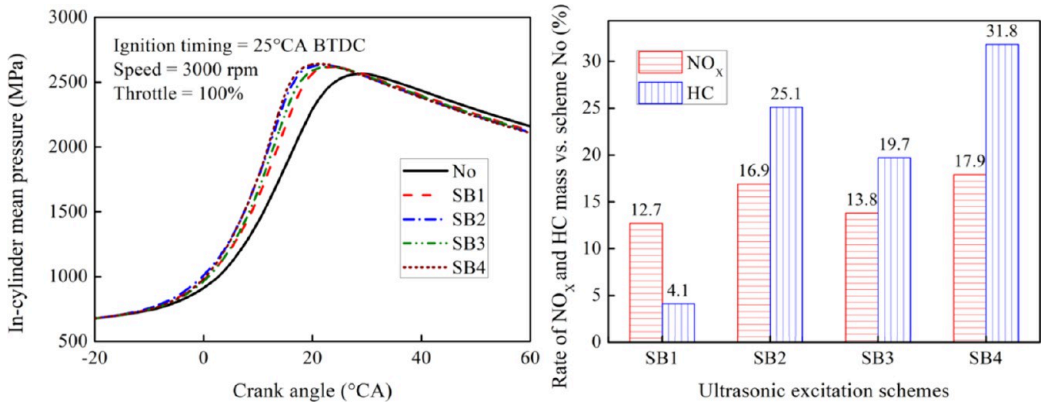

Figure 27. In-cylinder temperature and the variations of the NO_X and HC mass rates vs scheme No.

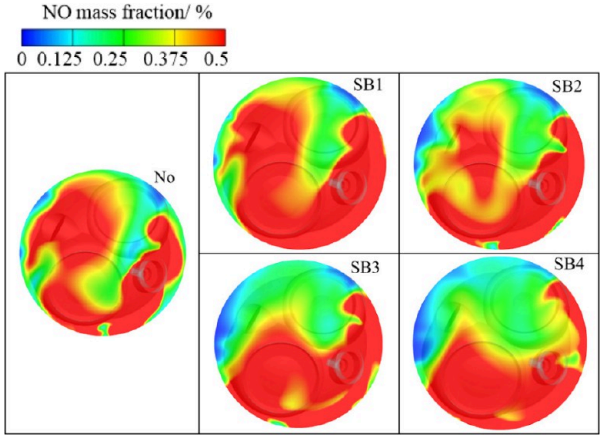

Figure 28. Distribution of NO at 120 °CA ATDC.

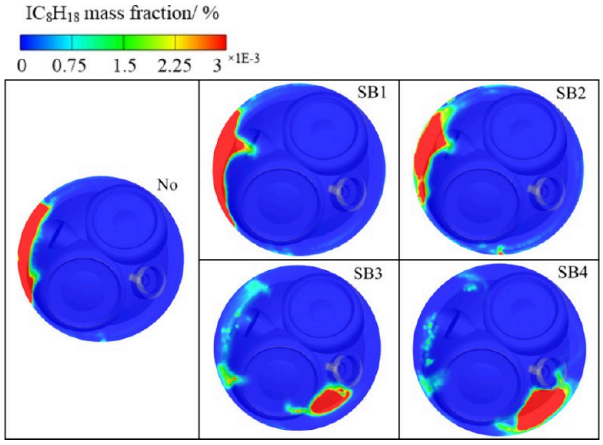

Figure 29. Distribution of IC_8H_{18} at 120 °CA ATDC.

6.6 J/°CA. Figure 25 describes the change in the combustion phase at different frequencies. It can be seen from the figure that there is little difference in combustion phase between frequencies of 20−50 kHz, which may be because although ultrasonic at a higher frequency can provide a higher TKE level, at the same time, it will also lead to a higher cyclic fluctuation so that the difference is not apparent.

Figure 26 compares the changes in cylinder P_{MAX} and IMEP at different frequencies. Compared with the scheme No, IMEP of the SB1−SB4 scheme increased by 1.2, 1.8, 1.3, and 1.7%, respectively. This indicates that under the full load condition of

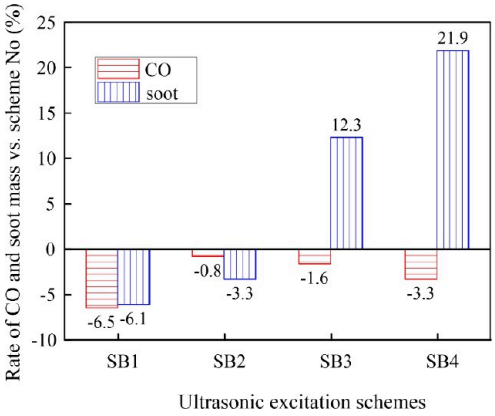

Figure 30. Variations of CO and soot mass rates at 120 °CA ATDC.

3000 r·min^{-1}, ultrasonic-fed can improve the combustion efficiency to a certain extent, but not the higher the frequency, the better the effect. SB2 (30 kHz) scheme has the largest IMEP improvement.

3.2.3. Effect of Variable Frequency Constant Amplitude Ultrasonic on Emission Formation. Figures 27 and 30show the rates of NO_X, HC, CO, and soot mass in the combustion chamber at 120 °CA ATDC. It can be seen from Figure 27a that in the frequency range of 20−50 kHz, the change of frequency has no significant influence on the combustion chamber temperature. It can be seen from Figure 27b that NO_X and HC rise as a whole but do not change linearly with an increase in frequency. According to the literature,[40] the main factors affecting the formation of NO_X are high temperature and oxygen enrichment in the combustion chamber. In the frequency range of 20−50 kHz, the increase of frequency increases the combustion temperature to a certain extent, thus promoting NO_X emissions. Figure 28 shows the spatial distribution of NO_X at 120 °CA ATDC. With an increased frequency, NO_X mainly concentrates on the spark plug side. The formation of HC belongs to the unburned part of the fuel. The simulation fuel uses IC_8H_{18}, so the IC_8H_{18} spatial distribution is used to explain the spatial distribution of HC, as shown in Figure 29. As can be seen from the figure, HC is mainly concentrated on one side of the sound source surface in the range of 20−30 kHz with no ultrasonic-fed and low frequency. This is because the addition of the sound source surface leads to excessive gaps in the combustion chamber, which directly deteriorates the near-wall fuel's combustion environment and is one of the main reasons for HC formation. In the high-frequency range of 40−50 kHz,

https://doi.org/10.1021/acsomega.3c05415
ACS Omega 2023, 8, 36418−36434

HC is mainly concentrated on the opposite side of the sound source surface (spark plug side), mainly because the higher the frequency, the more energy the sound wave transmits, blowing the fuel in the narrow gap to the other side. On the one hand, with the increase of frequency, the in-cylinder TKE is improved to a certain extent, which accelerates the flame propagation, and at the same time, the quenching phenomenon of the flame front impacting the wall is intensified. On the other hand, with the increase in frequency, the degree of cyclic fluctuation is amplified, resulting in strain flameout in the flame front, and this phenomenon becomes more serious with the increase in frequency. In the SB4 scheme, NO_X and HC increased by 17.9 and 31.8%, respectively. SB2 scheme followed by 16.9 and 25.1%. SB1 scheme is the least, accounting for 12.7 and 4.1%. SB3 is 13.8 and 19.7%. Among them, NO_X and HC increase the most in the SB4 scheme, up to 17.9 and 31.8%, respectively; SB2 scheme takes the second place, reaching 16.9 and 25.1%; SB1 scheme is the least, up to 12.7 and 4.1%; and SB3 is 13.8 and 19.7%.

According to the literature,[41] the key parameters influencing CO production are OH, O, and H active radical concentrations, as well as combustion temperature. Within the frequency range of 20−50 kHz, with the increase of frequency, the generation of active free radicals (as shown in Figure 23) and the combustion chamber temperature (as shown in Figure 27a) are improved to a certain extent, which promoted CO oxidation to a certain extent. Therefore, the emissions of CO in the SB1−SB4 scheme decreased. Among them, the SB1 (20 kHz) scheme decreased the most, up to 6.5%. SB1 and SB2 decreased by 6.1 and 3.3%. However, the soot formation of SB3 and SB4 increased significantly, reaching 12.3 and 21.9%, respectively. Therefore, under the same working conditions, excessive frequency increases will not bring good emissions.

4. CONCLUSIONS

(1) The influence of different ultrasonic amplitudes on combustion performance is studied by simulating ultrasonic-fed with a frequency of 20 kHz and amplitude of 30−300 μm. The greater the amplitude, the greater the influence on the in-cylinder flow field and the greater the influence on the combustion reaction rate and the faster the flame propagation speed. With the increase of amplitude, NO_X and HC emissions increase gradually and increase by 32.4 and 43.8% at 260 μm amplitude, respectively. Meanwhile, CO and soot emissions decreased gradually by 11.4 and 9%, respectively, when the amplitude is 260 μm.

(2) The influence of different ultrasonic frequencies on combustion performance is studied by simulating ultrasonic feeding with an amplitude of 100 μm and frequency of 30−50 kHz. The increase in frequency has an obvious influence on the in-cylinder flow field. When the frequency is between 30 and 50 kHz, wave propagation can be observed in the flow field area. With the increase of frequency, the flame propagation velocity increases, and ultrasonic has a negative effect on NO_X, HC, and soot formation, which increase by 31.8, 17.9, and 21.9%, respectively. CO emissions showed a downward trend but gradually slowed, with a maximum decline of 6.5%.

(3) Increasing the frequency and amplitude of ultrasonics can improve the combustion efficiency of the burner, but there is a difference between the two. The larger the amplitude, the higher the combustion efficiency, but the frequency is not. This is due to the fact that although the increase in frequency is conducive to the development of the turbulent motion of the combustion chamber, it in turn affects the development of the flame. However, the stronger the vibration, the more likely it is to quench the flame front, which has a negative effect on the combustion efficiency.

(4) In conclusion, the above simulation analysis is based on the full load condition of 3000 r·min^{-1}, and the analysis is made under the premise that ignition, fuel injection, and other control parameters of the original engine remain unchanged. It proves that ultrasonics has a regulation effect on emissions, and the degradation optimization of directional emissions can be realized through later optimization combined with the matching calibration of the ultrasonic-fed strategy.

AUTHOR INFORMATION

Corresponding Author

Liming Di − *School of Vehicle and Energy, Yanshan University, Qinhuangdao 066004, China; Hebei Key Laboratory of Special Delivery Equipment, Qinhuangdao 066004, China;* orcid.org/0000-0002-9533-426X; Email: diliming@ysu.edu.cn

Authors

Shiwei Zhang − *Zhengzhou Tourism College, Zhengzhou 450009, China*

Cheng Shi − *School of Vehicle and Energy, Yanshan University, Qinhuangdao 066004, China*

Complete contact information is available at: https://pubs.acs.org/10.1021/acsomega.3c05415

Notes

The authors declare no competing financial interest.

ACKNOWLEDGMENTS

This work was supported by the National Natural Science Foundation of China (Grant no. 51406174), Hebei Natural Science Foundation of China (Grant no. E2020203127), and Cultivation Project for Basic Research and Innovation of Yanshan University (Grant no. 2021LGZD014, 2021LGQN011).

NOMENCLATURE

ATDC: after top dead center
AMR: adaptive mesh refinement
BTDC: before top dead center
CA: crank angle
CFD: computational fluid dynamics
IMEP: indicated mean effective pressure
P_{MAX}: peak pressure
PRF: primary reference fuel
TDC: top dead center
TKE: turbulent kinetic energy
δ: total peak mass fraction of the OH, O, and H radicals
Φ: equivalence ratio
1d: one-dimension
3d: three-dimension

https://doi.org/10.1021/acsomega.3c05415
ACS Omega 2023, 8, 36418−36434

REFERENCES

(1) BLASING, T J. *Recent Greenhouse Gas Concentrations*; 2016. https://cdiac.ess-dive.lbl.gov/pns/current_ghg.html.

(2) METEOROLOGICAL, W., WMO, O. *WMO Statement on the State of the Global Climate in 2019*. 2019. https://public.wmo.int/en/media/news/un-secretary-general-will-launch-wmo-statement-state-of-global-climate-2019.

(3) CNPC Economics & Technology Research Institute. Energy Outlook of the World and China 2050 (2017 Edition). *Petrochemical Industry Application*IEEE 2017;*36*:149.

(4) Ministry of Ecology and Environment The People's Republic of China. *China Vehicle Environmental Management Annual Report (2018)*; Ministry of Ecology and Environment 2018.

(5) Ministry of Ecology and Environment The People's Republic of China. *Limits and Measurement Methods for Emissions from Light-Duty Vehicles (CHINA 6)*; Ministry of Ecology and Environment 2016.

(6) Bao, X.; Lv, M.; Zhu, R. Progress of Emission Control Standards for Light-Duty Vehicles in China. *J. Automot. Saf. Energy* **2017**, *8*, 213−25.

(7) Luo, H.; Yu, J.; Lou, H.; Huang, K.; Hu, J.; Xu, B. Thermal/Tribological Effects of Superimposed Ultrasonic Vibration on Viscoelastic Responses and Mold-Filling Capacity of Optical Glass: A Comparative Study. *Ultrasonics* **2020**, *108*, No. 106234.

(8) Sun, Z.; Wang, Y.; Xu, K.; Zhou, G.; Liang, C.; Qu, J. Experimental Investigations of Drilling Temperature of High-Energy Ultrasonically Assisted Bone Drilling. *Med. Eng. Phys.* **2019**, *65*, 1−7.

(9) Trimboli, P.; Bini, F.; Marinozzi, F.; Baek, J. H.; Giovanella, L. High-Intensity Focused Ultrasound (HIFU) Therapy for Benign Thyroid Nodules Without Anesthesia or Sedation. *Endocrine* **2018**, *61*, 210−5.

(10) Miller, D. L.; Lu, X.; Dou, C.; Zhu, Y. I.; Fuller, R.; Fields, K.; Fabiilli, M. L.; Owens, G. E.; Gordon, D.; Kripfgans, O. D.; et al. Ultrasonic Cavitation-Enabled Treatment for Therapy of Hypertrophic Cardiomyopathy: Proof of Principle. *Ultrasound Med. Biol.* **2018**, *44*, 1439−50.

(11) Sagin, S. V.; Solodovnikov, V. G. Cavitation Treatment of High-Viscosity Marine Fuels for Medium-Speed Diesel Engines. *Modern Appl. Sci.* **2015**, *9*, 269−278.

(12) Hong, L.; Hu, C. Rapid and Efficient Synthesis of 2-Phenyl Imidazolines under Ultrasonic Acceleration. *Hans J. Med. Chem.* **2017**, *5*, 11−51.

(13) Kamankesh, M.; Mohammadi, A.; Mollahosseini, A.; Jazaeri, S.; Shahdoostkhany, M.; et al. Vitamin D 3: Preconcentration and Determination in Cereal Samples Using 1 Ultrasonic-Assisted Extraction and Microextraction Method. *Cereal Chem. J.* **2017**, *94*, 532−8.

(14) Liu, L.; Du, M.; Li, G.; Fan, J.; Schobert, H. H.; He, C.; et al. Study on the Small Molecular Composition of Cutinite from Luquan Cutinitic Liptobiolith by Ultrasonic-Assisted Sequential Extraction. *Energy Fuels* **2019**, *33*, 3465−72.

(15) Fujisawa, N.; Iwasaki, K.; Fujisawa, K.; Yamagata, T.; et al. Flow Visualization Study of a Diffusion Flame under Acoustic Excitation. *Fuel* **2019**, *251*, 506−13.

(16) Jocher, A.; Foo, K. K.; Sun, Z.; Dally, B.; Pitsch, H.; Alwahabi, Z.; Nathan, G.; et al. Impact of Acoustic Forcing on Soot Evolution and Temperature in Ethylene-Air Flames. *Proc. Combust. Inst.* **2017**, *36*, 781−8.

(17) Oh, J.; Heo, P.; Yoon, Y. Acoustic Excitation Effect on NOx Reduction and Flame Stability in a Lifted Non-Premixed Turbulent Hydrogen Jet with Coaxial Air. *Int. J. Hydrogen Energy* **2009**, *34*, 7851−61.

(18) Hassan, M. I.; Wu, T. W.; Saito, K. A Combination Effect of Reburn, Post-Flame Air and Acoustic Excitation on NOx Reduction. *Fuel* **2013**, *108*, 231−7.

(19) Deng, K.; Shen, Z.; Wang, M.; Hu, Y.; Zhong, Y. j.; et al. Acoustic Excitation Effect on NO Reduction in a Laminar Methane-Air Flame. *Energy Proc.* **2014**, *61*, 2890−3.

(20) Deng, K.; Wang, M.; Shen, Z.; Hu, Y.; Zhong, Y.; et al. Effect of Different Acoustic Parameters on NOx Emissions of Partially Premixed Flame. *Appl. Sci.* **2019**, *9*, 1490.

(21) Pereira, A. R. B.; Santos, A. Á. B.; Guarieiro, L. L. N.; Cavalcante, J. B. H.; dos Anjos, J. P.; et al. Experimental Evaluation of CO, NOx, Formaldehyde and Acetaldehyde Emission Rates in a Combustion Chamber with OEC under Acoustic Excitation. *Energy Rep.* **2019**, *5*, 1163−71.

(22) Ion, I. V.; Dimofte, E.; Popescu, F.; Akhmetova, I. G.; et al. Investigation of Flame Acoustic Excitation of a Gas Burner. *Energy Rep.* **2022**, 263−9.

(23) Long, X.; Gou, X. Lifted-off Flame Mechanism of N-heptane Droplet Combustion in Ultrasonic Field. *J. Combust. Sci. Technol.* **2020**, *26*, 558−66.

(24) Di, L.; Sun, W.; Sun, T.; et al. Study on Spatial Location Ignition of Flammable Mixtures Based on Spherical Focused Ultrasound. *J. Combust. Sci. Technol.* **2021**, *27*, 493−500.

(25) Di, L.; Zhang, S.; Shi, C.; Sun, Z.; Ouyang, Q.; Zhi, F.; Yang, Q.; et al. Effect of ultrasonic-fed time on combustion and emissions performance in a single-cylinder engine. *Chemosphere* **2022**, *302*, No. 134924.

(26) Fan, B.; Pan, J.; Yang, W.; Liu, Y.; Bani, S.; Chen, W.; et al. Numerical Investigation of the Effect of Injection Strategy on Mixture Formation and Combustion Process in a Port In-jection Natural Gas Rotary Engine. *Energy Convers. Manage.* **2017**, *133*, 511−23.

(27) Binjuwair, S., Ibrahim, S. *Numerical Analysis of Flow Structure Inside a Single Cylinder of a 4 Valve Head Under Steady-state Condition*. SAE Technical Paper 2013-24−0186,2013.

(28) Han, Z.; Reitz, R. D. A Temperature Wall Function Formulation for Variable-density Turbulent Flows with Application to Engine Convective Heat Transfer Modeling. *Int. J. Heat Mass Transf.* **1997**, *40*, 613−25.

(29) Spreitzer, J., Zahradnik, F., Geringer, B. *Implementation of a Rotary Engine (Wankel Engine) in a CFD Simulation Tool with Special Emphasis on Combustion and Flow Phenomena*; SAE Technical Paper 2015-01−0382,**2015**.

(30) Rao, V.; Honnery, D. A Comparison of Two NOx Prediction Schemes for Use in Diesel Engine Thermodynamic Modelling. *Fuel* **2013**, *107*, 662−70.

(31) Jabbr, A. I.; Koylu, U. O. Influence of Operating Parameters on Performance and Emissions for a Compression-ignition Engine Fueled by Hydrogen/Diesel Mixtures. *Int. J. Hydrogen Energy* **2019**, *44*, 13964−73.

(32) Liu, Y. D.; Jia, M.; Xie, M. Z.; Pang, B.; et al. Enhancement on a Skeletal Kinetic Model for Primary Reference Fuel Oxidation by Using a Semidecoupling Methodology. *Energy Fuels* **2012**, *26*, 7069−83.

(33) Du, J.; Chen, F. Cavitation Dynamics and Flow Aggressiveness in Ultrasonic Cavitation Erosion. *Int. J. Mech. Sci.* **2021**, *204*, No. 106545.

(34) Dabir-Moghaddam, N.; Song, H.; Wu, B. Modeling of Cavitating Flow Induced by an Ultrasonic Horn above a Solid Target with a Microhole. *J. Manuf. Process.* **2018**, *32*, 327−36.

(35) Chen, F.; Du, J.; Zhou, S. Cavitation Erosion Behaviour of Incoloy Alloy 865 in NaCl Solution Using Ultrasonic Vibration. *J. Alloys Compd.* **2020**, *831*, No. 154783.

(36) Yusuf, L.; Symes, M. D.; Prentice, P. Characterising the Cavitation Activity Generated by an Ultrasonic Horn at Varying Tip-Vibration Amplitudes. *Ultrasonics Sonochem.* **2021**, *70*, No. 105273.

(37) Taghavifar, H.; Khalilarya, S.; Jafarmadar, S. Engine Structure Modifications Effect on the Flow Behavior, Combustion, and Performance Characteristics of DI Diesel Engine. *Energy Convers. Manage.* **2014**, *85*, 20−32.

(38) Abdul Gafoor, C. P.; Gupta, R. Numerical Investigation of Piston Bowl Geometry and Swirl Ratio on Emission from Diesel Engines. *Energy Convers. Manage.* **2015**, *101*, 541−51.

(39) Shi, C.; Ji, C.; Ge, Y.; Wang, S.; Yang, J.; Wang, H.; et al. Effects of Split Direct-Injected Hydrogen Strategies on Combustion and Emissions Performance of a Small-Scale Rotary Engine. *Energy* **2021**, *215*, No. 119124.

https://doi.org/10.1021/acsomega.3c05415
ACS Omega 2023, 8, 36418−36434

(40) Huang, H.; Liu, Q.; Yang, R.; Zhu, T.; Zhao, R.; Wang, Y. Investigation on the Effects of Pilot Injection on Low Temperature Combustion in High-Speed Diesel Engine Fueled with n-Butanol−Diesel Blends. *Energy Convers. Manage.* **2015**, *106*, 748−58.
(41) Zhu, J.; Huang, H.; Zhu, Z.; Lv, D.; Pan, Y.; Wei, H.; Zhuang, J. Effect of Intake Oxygen Concentration on Diesel-n-Butanol Blending Combustion: An Experimental and Numerical Study at Low Engine Load. *Energy Convers. Manage.* **2018**, *165*, 53−65.

https://doi.org/10.1021/acsomega.3c05415
ACS Omega 2023, 8, 36418−36434